Role of the charge state of interface defects in electronic inhomogeneity evolution with gate voltage in graphene

Anil Kumar Singh and Anjan K. Gupta
Department of Physics, Indian Institute of Technology Kanpur, Kanpur 208016, India

(Received 19 August 2017; revised manuscript received 16 April 2018; published 9 May 2018)

Evolution of electronic inhomogeneities with back-gate voltage in graphene on SiO_2 was studied using room temperature scanning tunneling microscopy and spectroscopy. Reversal of contrast in some places in the conductance maps and sharp changes in cross correlations between topographic and conductance maps, when graphene Fermi energy approaches its Dirac point, are attributed to the change in charge state of interface defects. The spatial correlations in the conductance maps, described by two length scales, and their growth during approach to Dirac point, show a qualitative agreement with the predictions of the screening theory of graphene. Thus a sharp change in the two length scales close to the Dirac point, seen in our experiments, is interpreted in terms of the change in charge state of some of the interface defects. A systematic understanding and control of the charge state of defects can help in memory applications of graphene.

DOI: 10.1103/PhysRevB.97.195415

I. INTRODUCTION

Potential landscape created by charged defects buried in the substrate and at graphene-substrate interface leads to carrier density inhomogeneities in graphene devices. Such inhomogeneities have been observed experimentally in graphene on SiO_2 substrate by scanning single-electron transistor and scanning tunneling microscopy and spectroscopy (STM/S) [1–4]. The inhomogeneity is undesired as it limits the carrier mobility and restricts one from precisely accessing the Dirac point due to electron-hole puddle formation [5]. Thus several research groups have moved away from devices having graphene-SiO_2 interface as amorphous SiO_2 shelters many defects, particularly near the surface where graphene is placed. As a result of change in charge state of intrinsic defects and extrinsic species at the graphene-SiO_2 interface, the field electron devices with SiO_2 gate dielectric show significant hysteresis [6]. The hysteresis, on the other hand, offers application potential in data storage. Thus understanding these interface charge traps, particularly for finding ways to control and probe the charge stored in them, is important.

Zhang *et al.* [2] found that the presence of charge-donating impurities below graphene lead to the formation of standing wave patterns by backscattering of Dirac fermions. Gibertini *et al.* [7] reported that corrugations in graphene are sufficient for the formation of electron-hole puddles. Dielectric screening properties of graphene have been discussed by several groups [8–11] to understand electron-hole puddle formation. Self consistent linear screening theory with random phase approximation (RPA) [10,12] was used by Samaddar *et al.* [13] to model the observed growth in the length scale of charge inhomogeneities in graphene. A general qualitative agreement with the screening theory was found by these authors [13] but with a few unexplained features, such as asymmetry in the correlation length behavior between the electron and hole doping and the relatively poor fit of the conductance auto-correlations with a single Gaussian function. The defects can also change their charge state by exchanging electrons with graphene thus affecting the carrier density as well as inhomogeneities. Depending on the overlap of defect states with graphene and temperature, this electron transfer can be dominated either by thermal activation or tunneling. Finite temperature also affects screening properties due to thermally activated electron-hole pairs, and thus at room temperature the screening properties for carrier density below 10^{11} cm^{-2} are expected to differ from those of zero temperature [14].

In this paper we report on the role of back-gate dependent charge state of interface defects in the evolution of electronic inhomogeneities in single layer graphene on SiO_2 with back-gate-voltage (V_g). The evolution of the conductance and topographic maps with V_g is studied using a room temperature vacuum STM. The cross-correlation between topography and conductance maps of different V_g values show abrupt change as E_F approaches the Dirac point in addition to an increase in the length scales associated with charge inhomogeneity. Following Samaddar *et al.* [13] we analyze the auto-correlation maps and find two length scales, instead of one, near the Dirac point. From the evolution of local correlations in conductance maps with gate voltage we clearly see some of the regions reversing their contrast and some preserving it. Further, the conductance maps are described by two length scales, and both grow as E_F approaches the Dirac point with some abrupt changes. The latter is discussed in terms of the change in the charge state of some of the defects.

II. EXPERIMENTAL DETAILS

Graphene flakes were mechanically exfoliated from kish graphite using an adhesive tape on 300 nm thick SiO_2 on top of n-doped silicon substrate. Optical contrast and Raman spectra of graphene flakes on SiO_2/Si substrate were used to identify the single layer graphene. A mechanical wire masking method was used to make contacts of Cr(10 nm)/Au(50 nm)

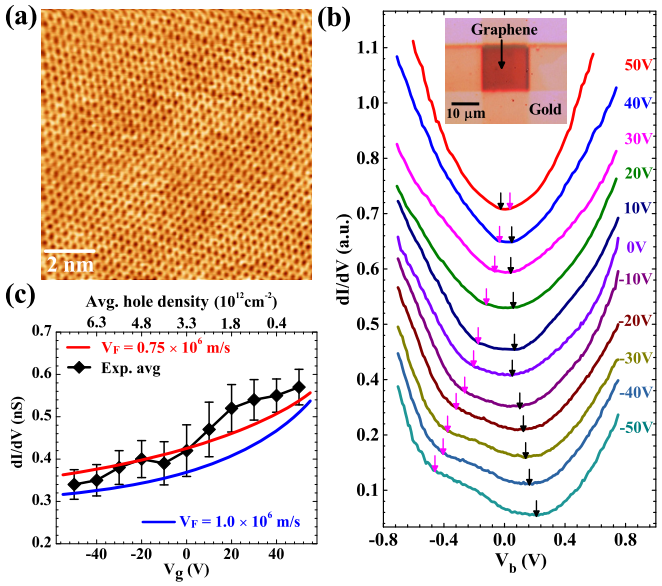

FIG. 1. (a) An STM image (11.2×11.2 nm^2, 0.3 V/0.1 nA) of sample 1 showing the atomically resolved honeycomb lattice of graphene. (b) shows the local tunneling conductance spectra (0.8 V/0.1 nA) at different V_g values taken at a fixed location on graphene. The black arrow in each spectrum marks the minimum location while the purple arrow indicates the second shoulderlike feature. The inset in (b) shows the studied graphene sample surrounded by gold film on top. In (c) the continuous lines show the calculated dependence of conductance on V_g (see text for details) while the discrete points (diamonds) show the average conductance found from STS maps with the bars depicting the standard deviation of the maps.

on graphene. We used a homemade room temperature STM, with a 2D nano positioner [15] sample holder. The STM is kept inside a vacuum chamber pumped by a cryopump with pressure in 10^{-4} mbar range throughout the measurement. The gate voltage was applied on Si substrate with a 10 kΩ series resistance. Details of the device fabrication and measurement are same as those described elsewhere [16].

We performed STM/S studies on several monolayer graphene samples in different regions away from the metal-graphene contact interface. Here we present two data sets (1 and 2) on different samples with both showing qualitatively similar behavior. Small-scale, see Fig. 1(a), topographic images of all studied samples show atomically resolved surface. The V_g dependent local tunnel-conductance spectra (on sample 1) in Fig. 1(b) show one minima and a second shoulderlike feature due to tip-doping effects [13,16–18]. The second feature is often seen as a full minima in some of the spectra. The two features move towards each other when V_g increases from -50 to 50 V; they eventually merge close to $V_g = 50$ V implying significant p doping with hole density of order 4×10^{12} cm^{-2}. Qualitatively similar spectra were seen over a large area of the sample with the major difference being the slight variation in V_b position of the two features at fixed V_g. We have occasionally seen three features, i.e. a primary minima with two secondary shoulders around it, in local spectra. This can be understood from the energy localized interface states as discussed in our recent work [16]. Similar doping is seen in the two probe resistance of an identically prepared sample [19]. We could not measure the resistance of the device that was used for STM/S study as the Au/Cr contact was deposited on all sides of graphene as shown in the inset of Fig. 1(b).

Interpretation of STS maps

Potential or carrier density inhomogeneity can be mapped in several ways using STS. One way is to acquire full tunneling conductance spectrum at each pixel with open feedback in current imaging tunneling spectroscopy mode, which is comprehensive but demanding in terms of amount of data and time. We acquired spatial maps of dI/dV at a fixed bias (V_b) and in a closed feedback loop, with large integration time, using Lock-in method with an ac modulation (2.731 kHz, 20 mV rms). Figure 1(b) shows local dI/dV spectra at different V_g. Besides the minimum marked by a black arrow, a shoulderlike feature is visible at very negative V_g (purple arrow at -50 V). This feature can be followed as an abrupt slope change at less negative V_g indicating that the feature is moving oppositely with V_g than the minimum of the dI/dV curve. In Ref. [17], we have correlated the additional feature at the purple arrow, with the tip voltage, where the Dirac point is identical to the Fermi level of graphene due to the combined gating by back gate and tip voltage (V_b), while the minimum at the black arrow marks the Dirac point energy caused mostly by back gating. Here, we use the V_g dependence of the two features to estimate the tip-sample distance by a capacitive model [17] revealing the tip-sample separation $z = 0.9 \pm 0.1$ nm. We note that as compared to the tunneling gap this overestimates the separation as the tunneling is confined to the tip apex as compared to the capacitive coupling. However, we concentrate on the V_b region larger than the minima position marked by the black arrow in order to track the unperturbed local Dirac point energy as a function of V_g.

From the spectra the minima movement in this sample occurs between V_b values of 0 and 0.2 V and the second feature remains at negative V_b for the studied V_g range. So, for STS maps, we choose $V_b = 0.25$ V to avoid either of the two minima crossing this bias value for studied V_g values. We approximate the low bias portion of the differential tunnel conductance by a parabola, i.e., $G(V_b, V_D) = G_0[1 + G_1(V_b - V_D)^2]$. Here V_D is the location of the primary minima with eV_D as the energy of the Dirac point from the Fermi energy. Thus $V_D > 0$ represents a hole doped graphene spectrum. G_0 and G_1 are found by fitting the bottom portion of the local spectra [19].

The conductance maps are acquired in closed-feedback-loop mode with fixed tunnel current (0.1 nA) and V_b values. Thus the variation in local conductance occurs due to V_D inhomogeneity. We can write the measured local conductance in the STS maps acquired using this modulation technique as $G_{\mathrm{STS}}(V_D) = \frac{I(V_b,0)}{I(V_b,V_D)} G(V_b, V_D)$ with $I(V_b, V_D) = \int_0^{V_b} G(V, V_D) dV$. Further, attributing the local V_D or n, i.e., electron density, to V_g, V_b, and a local potential V_g^D, we get $n = \frac{\kappa \epsilon_0}{ed}(V_g - V_g^D - \frac{d}{\kappa z} V_b)$. Here, V_g^D arises due to the screened potential of defect charges (at the interface) and the contact potential difference between the tip and graphene. Thus,

$$V_D = -\mathrm{Sgn}(n) \frac{\hbar v_F}{e} \sqrt{\pi |n|}. \quad (1)$$

Here, $\kappa = 4$ and $d = 300$ nm are the dielectric constant and thickness of SiO_2 layer, respectively. We use $V_g^D = 50$ V, i.e., close to the doping seen in spectra, and $z = 0.9$ nm. Figure 1(c) shows the conductance, thus calculated, for $v_F = 1 \times 10^6$ and 0.75×10^6 m/s. The discrete points in this plot show the V_g dependent average conductance as found from the conductance maps (2) for comparison. An apparent reduction in v_F can be attributed to screening of gate electric field by the interface defects [16], which happens by way of defects changing their charge state as discussed here in more detail.

With a fixed V_g^D value, the above calculated conductance variation with V_g ignores any V_D change due to the change in the charge state of the defects. The electronic inhomogeneity, attributed to V_g^D variation, gives rise to a spread in conductance. The standard deviation due to this spread is depicted as error bars in Fig. 1(c). The continuous line in this plot can be used to convert the conductance maps to carrier density maps using the scale shown on the top of this plot. Since this plot is monotonically rising, the conclusions drawn using the spatial correlations and associated length scales of conductance will not be affected. This plot also gives a method to interpret the conductance contrast, such as the nature (electron- or hole-type) of charge puddles and their evolution with V_g.

III. STS STUDY OF ELECTRONIC INHOMOGENEITY

Figure 2 shows the STS conductance maps at different V_g between ± 50 V together with the simultaneously taken topography images. The small scale topographic images in the same region, see Fig. 1(a), show the honeycomb structure of graphene. All the images in Fig. 2 correspond to the same area of the sample. This was ensured by finding the (small) relative shifts between topographic images of different V_g by using the cross-correlation maps. The largest common area was then cropped from both the topography and conductance maps taken at different V_g. It can be seen from Fig. 2 that the topography images do not change noticeably with V_g while there are significant changes in the conductance maps, particularly when V_g approaches $+50$ V, see Figs. 2(a) and 2(k). This implies that the contribution to the topographic contrast from electronic inhomogeneity is insignificant and these images reflect the actual topography of the surface as arising from the underlying SiO_2 [20,21]. On the other hand, there is a clear anticorrelation between the topography and conductance images, see Fig. 2(l), particularly for negative V_g values. This implies that the charged defects at the interface, responsible for electronic contrast, have some correlation with the topography [7].

From Fig. 1(c), we deduce that the dark regions of an STS image represent high hole-density regions. Thus for the STS maps close to $V_g = 50$ V, when graphene's E_F coincides with its Dirac point on average, the dark (bright) regions would represent hole (electron) puddles. Also at large positive V_g the interface defects will have a tendency to acquire negative charge. The graphene region close to such defects will have smaller electron density as compared to average electron density. Thus the electron puddles (above the positively charged defects) will have a tendency to disappear (or change to hole puddles) as V_g approaches $+50$ V. At the same time some of the average carrier density regions (above neutral defects) will become hole puddles. The hole puddles (above negatively

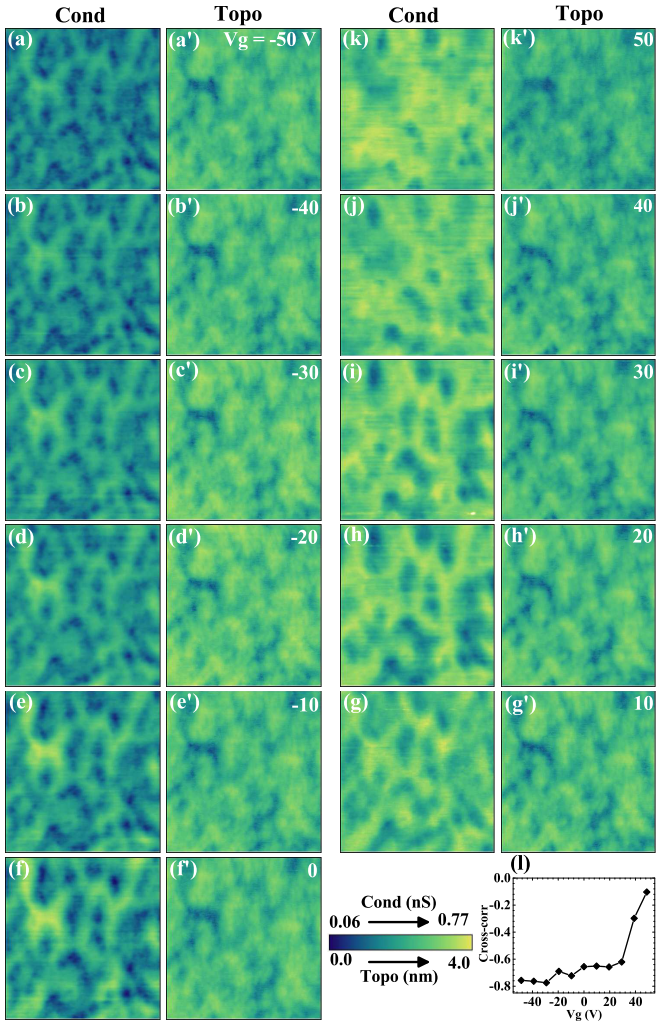

FIG. 2. (a) to (k) show the conductance maps depicting electron inhomogeneities with (a′) to (k′) showing corresponding topographic maps over an area of 120×120 nm^2 at different V_g values. Imaging parameter for all the maps are bias voltage $V_b = 0.25$ V and current set point 0.1 nA. (l) shows the cross-correlation coefficient between the conductance and topographic maps as a function of V_g.

charged defects) are unlikely to change in this sense. It has been proposed that a good number of defects have their ionization energies pinned close to the Dirac point of graphene [16,22–24] and thus the change in their ionic state will occur when V_g is close to 50 V.

We can see several regions in the STS images in Fig. 2 that retain their contrast even up to $V_g = +50$ V while there are some that change to opposite contrast. To see these local correlations clearly, we show, in Fig. 3(a), the product of the $V_g = +50$ and -50 V STS maps after average subtraction and normalization by standard deviation. The average of this product map gives the cross correlation of the two maps [$A(0,0)$ with respect to Eq. (2)], which is close to -0.2, see Fig. 3(b). The normalization also ensures that the average of this image lies between $+1$ and -1 with these two limits corresponding to a perfect correlation and anticorrelation, respectively. Thus the contrast in this product map is a good measure of local correlations and anticorrelations. There are some prominent

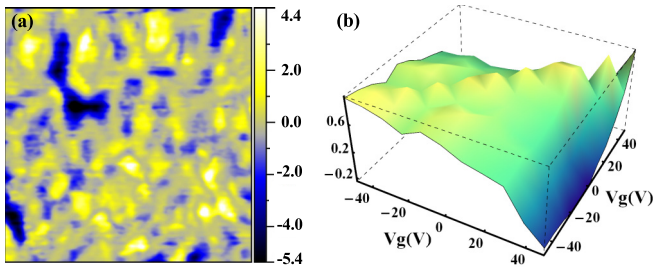

FIG. 3. (a) shows the product image of the conductance maps (after average subtraction and division by standard deviation of respective maps) of $V_g = +50$ and -50 V. (b) shows a 3D rendering of cross-correlation coefficients between different V_g conductance maps as a function of gate voltage.

bright and dark regions in Fig. 3(a) with the former (latter) indicating position of defects that maintain (change) their charge state. The dark (anticorrelated) regions of the product map can arise either from bright becoming dark or from dark becoming bright. As seen from Figs. 2(a) and 3(a), bright becoming dark dominates. Also the bright regions of the product map can come from bright remaining bright or dark remaining dark. The latter dominates, when V_g changes from -50 to $+50$ V. Figure 3(b) shows the cross correlation coefficients between different STS maps, which is seen to be more than $+0.5$ except for $V_g = 40$ and 50 V. The abrupt jump around $V_g = 40$ V is again believed to occur due to defect-state change. This is a qualitative conclusion and more detailed evolution of this contrast will depend on the detailed distribution of the two types of defects. The evolution of contrast and the size of the electron and hole puddles will also depend on the screening properties of graphene as discussed later.

Sample 2 shows a similar behavior in terms of local contrast evolution in STS maps with V_g [19] and the correlation between the topographic and conductance maps. In addition, in this sample we find that the STS maps show some sort of instability in the vicinity of the point when E_F coincides with the Dirac point. This could occur due to tip-induced change in the charge state of interface defects. The tip, with bias V_b, can also lead to change in charge state of interface defects by way of tip-doping effects. The stability of the STS images will be dictated by the competition between the rate of charge-state change and the tip scan rate. The former rate can, in fact, be very slow [25] and thus slowing down the scan speed may not be a practical solution for getting stable images.

We would also like to point out that for sample 1 the STM/S images were taken in the V_g sequence $+40$ to -50 V and then $+50$ V, i.e., Figs. 2(j) to 2(a) and then 2(k). Looking at the continuity between the $+40$ V and $+50$ V STS images taken after full V_g cycle we do not see any visible signatures of hysteresis, which is anyway seen to be quite small from the transport measurements on similarly prepared samples [19]. The hysteresis is believed to arise from the metastability of the charge state of defects near the graphene-SiO_2 interface [25]. Our STS measurements are quite slow in the sense that each image takes about an hour to complete. In addition, the tip (with a bias voltage) can also help in relaxing the local defects out of the metastable state.

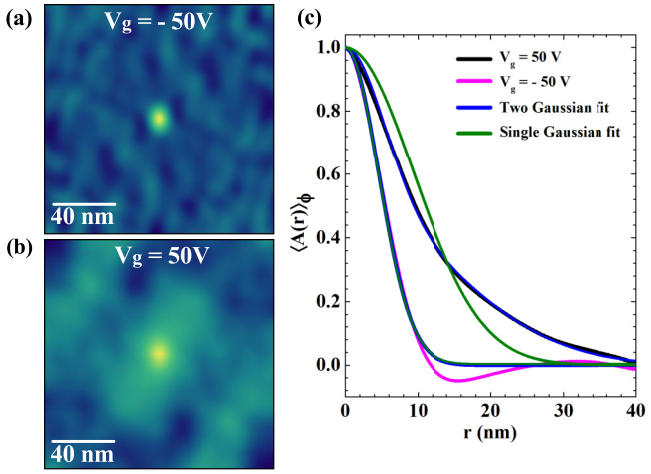

FIG. 4. (a) and (b) show the autocorrelation maps, calculated using Eq. (2), of conductance images at $V_g = -50$ and $+50$ V, respectively. (c) shows angular average of the line cut passing through the center of (a) and (b) with its single and double Gaussian fits.

Puddle size evolution

To quantify the electronic inhomogeneity length scale (or puddle size) and analyze its evolution with V_g we filtered all the images using a Gaussian filter of 1 nm width before calculating correlations. We find the cross correlation $A(x,y)$ between two experimentally acquired images, i.e., $z_{1,2}(i,j)$, using

$$A(i,j) = \frac{\sum_{i',j'} z_1(i',j') z_2(i+i', j+j') - \langle z_1\rangle\langle z_2\rangle}{\sqrt{\left[\left(\langle z_1^2\rangle - \langle z_1\rangle^2\right)\left(\langle z_2^2\rangle - \langle z_2\rangle^2\right)\right]}}. \quad (2)$$

Here the sum over i' and j' and the averages ($\langle \ldots \rangle$) are evaluated over the overlapping area after the relative shift by i and j. The same is used for finding the autocorrelation. With this expression the cross correlation will be normalized, i.e., it will give a value $+1$ for perfect correlation, zero for no correlation, and -1 for perfect anticorrelation. Thus an autocorrelation image will have value $+1$ at the origin. A Mathematica program was written to calculate the autocorrelation images using Eq. (2).

A line cut in this cross correlation function A(x,y) through the origin can be represented by $A(r,\phi)$ along a fixed direction ϕ. Angular averaged, normalized correlation function $\langle A(r)\rangle_\phi$ can be fitted to a Gaussian function or a combination of Gaussian functions of the form $\exp[-r^2/2\xi^2]$ with ξ as correlation length. The error bars in various fitting parameters were found in the same way as those by Samaddar *et al.* [13], i.e., from the extreme values of the fitting parameters with respect to ϕ. Figure 4(a) shows the autocorrelation image of dI/dV image at $V_g = -50$ V. This image shows a sharp peak at origin with certain decay length ξ. The $V_g = 50$ V autocorrelation in Fig. 4(b) shows a sharp decay, i.e., a small correlation length, followed by a gradual decay, i.e., a large correlation length. This is clear from $\langle A(r)\rangle_\phi$ shown in Fig. 4(c). We have fitted this $\langle A(r)\rangle_\phi$ with single Gaussian function $\exp[-r^2/2\xi^2]$ as well as with a sum of two Gaussian functions, i.e.,

$$\langle A(r)\rangle_\phi = \sigma \exp\left[-r^2/2\xi_1^2\right] + [(1-\sigma)\exp\left[-r^2/2\xi_2^2\right]. \quad (3)$$

At $V_g = -50$ V, the $\langle A(r)\rangle_\phi$ fits well with a single Gaussian whereas for $V_g = 50$ V it has large deviation from a single Gaussian. But both the curves can be fitted well by sum of two Gaussian functions.

The presence of two length scales near the Dirac point can be seen directly from the conductance map in Fig. 2(k) from a few scattered small-size dark spots in a relatively flat and bright looking background. The dark spots can arise from segregated defect clusters giving small hole puddles in a well connected electronlike landscape. Such two different size puddles in potential landscape are also anticipated in an effective medium theory [26]. The presence of two length scales near Dirac point is also found to be valid for the STS images of sample 2 [19], as per Fig. 6(b), in which the charge neutrality point appears close to $V_g = 15$ V. In order to discuss the V_g evolution of these length scales we first briefly discuss the predictions of linear screening theory of defect potential in graphene.

IV. LINEAR SCREENING THEORY OF ELECTRONIC INHOMOGENEITY

The Thomas-Fermi wave vector q_{TF} in graphene is proportional to the square root of the carrier density. As a consequence the unscreened potential created by charge impurities and screened potential are identical at Dirac point and the screening length q_{TF}^{-1} strongly depends on the carrier density. For a random distribution of charged impurities with density $n_{\rm imp}$ in a plane at distance d from the graphene sheet, the screened impurity potential is given by [10],

$$C(r) = 2\pi n_{\rm imp}\left(\frac{e^2}{4\pi\epsilon_0\kappa}\right)^2 \int_0^\infty \left[\frac{1}{\epsilon(q)}\frac{e^{-qd}}{q}\right]^2 J_0(qr)qdq. \tag{4}$$

Here κ is the bulk (3D) dielectric constant, J_0 is the zeroth-order Bessel function, e is the magnitude of electronic charge and $\epsilon(q)$ is the temperature dependent graphene dielectric function. Normalized correlation function $A(r) = C(r)/C(0)$ is more useful for describing the spatial profile of the screened impurity potential or electron-hole puddles while $C(0)$ characterizes the mean-square potential fluctuations, i.e., $\tilde{V}^2_{rms}$. $A(r)$ has a Gaussian-like appearance, i.e., $\exp[-r^2/2\xi^2]$ with ξ as a correlation length.

To find the variation of correlation length(s) with $n_{\rm imp}$, d, and n_g, we calculated $A(r)$ using the $\epsilon(q)$ corresponding to linear screening theory with random phase approximation [10,11,19] for fixed $T = 300$ K. Here, $n_g = \frac{\kappa\epsilon_0}{ed}V_g$ is the carrier density due to the gate voltage. Figure 5(a) shows $A(r)$ for $n_{\rm imp} = 5\times10^{11}$ cm^{-2}, $d = 1.0$ nm, and for two different carrier density (n_g) values together with their fits to single and double Gaussian [see Eq. (3)]. Clearly the double Gaussian fit is much better, which is found to be the case for a wide range of $n_{\rm imp}$, d, and n_g values. The discrepancy of $A(r)$ with its single Gaussian fit was found to be more pronounced at small n_g and large d values. In fact, the effective medium theory, near the Dirac point, by Rossi *et al.* [26], which includes the nonlinear screening and exchange-correlation effects, also finds two distinct length scales in the screened potential.

Figure 5(b) shows the calculated variation of ξ_1 and ξ_2 with $n_{\rm imp}$ at small n_g. Both lengths decrease with $n_{\rm imp}$ but

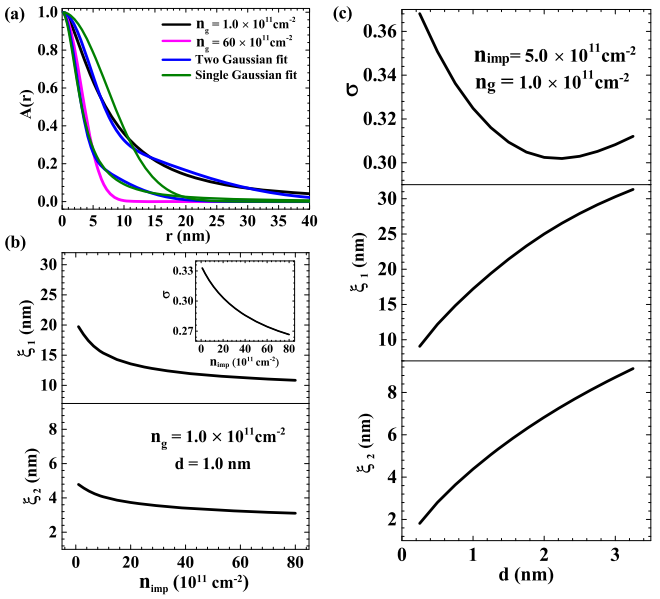

FIG. 5. (a) Single and two Gaussian fits of theoretically calculated A(r) at $d = 1.0$ nm and $n_{\rm imp} = 5\times10^{11}$ cm^{-2} for low n_g ($\xi = 7.2$ nm, $\sigma = 0.32$, $\xi_1 = 17.2$ nm, $\xi_2 = 4.4$ nm) and high n_g ($\xi = 3.1$ nm, $\sigma = 0.24$, $\xi_1 = 7.9$ nm, $\xi_2 = 2.2$ nm). (b) shows the evolution of ξ_1 and ξ_2 as a function of $n_{\rm imp}$ at $d = 1.0$ nm; inset shows σ as a function of $n_{\rm imp}$. (c) shows the evolution of σ, ξ_1, and ξ_2 as a function d at $n_{\rm imp} = 5\times10^{11}$ cm^{-2}.

the variation in ξ_2 with $n_{\rm imp}$ is much smaller as compared to that in ξ_1 for a given d. Figure 5(c) shows d dependence of $\xi_{1,2}$, at small n_g, with both showing a significant increase with d. n_g dependence of $\xi_{1,2}$ [19] for different $n_{\rm imp}$ and d shows a decrease in both as we move away from the Dirac point. Mathematically $A(r)$, and thus $\xi_{1,2}$, evolve differently with d and q_{TF}^{-1}, with the later dependent on $n_{\rm imp}$, n_g, and d. ξ_1 has a noticeable dependence on all three parameters, i.e., d, n_g, and $n_{\rm imp}$, while ξ_2 has noticeable dependence on d but it has relatively weak dependence on n_g and $n_{\rm imp}$, which play a somewhat similar role as both dictate the average carrier density [10].

V. V_g EVOLUTION OF ξ: SCREENING AND DEFECTS' CHARGE STATE

Figure 6(a) shows the V_g dependence of $\xi_{1,2}$, σ, and ξ as found using the STS images, shown in Fig. 2, of sample 1. Here ξ corresponds to the single Gaussian fit. ξ_1 and ξ_2, found from two Gaussian fitting, are differentiated by their magnitudes and smooth variation of each with V_g. When σ takes values close to 0 or 1, the single Gaussian was found to fit $A(r)$ quite well. This can be easily understood from Eq. (3). Away from the Dirac point a single Gaussian with length ξ fits $A(r)$, and ξ grows when the Dirac point is approached. Similar behavior can be seen for sample 2 (with Dirac point at $V_g \sim 15$ V) in the sense that a single Gaussian fits away from the Dirac point and $\xi_{1,2}$ or ξ grow as E_F approaches the Dirac point. In fact the variation of $\xi_{1,2}$, particularly in the regime where two Gaussians fit better, is rather abrupt as compared to what is expected from the model [19]. Incidently, the correlation length

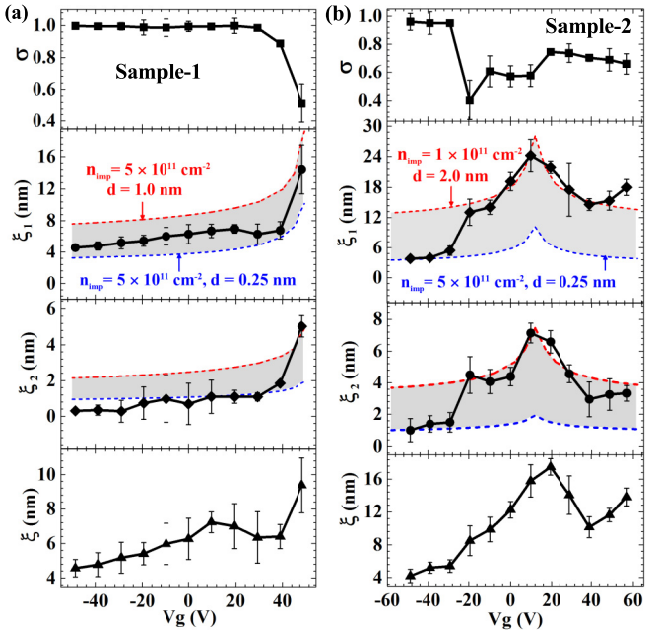

FIG. 6. Evolution of σ, ξ_1, ξ_2, and ξ as a function of gate voltage V_g extracted from conductance maps of (a) sample 1 and (b) sample 2. The gray shaded region can be accessed by choosing appropriate $n_{\rm imp}$ and d values in a range defined by these parameters for the blue and red limiting lines that have been calculated using the screening theory. The error bars in these fitted parameters were found from the extreme values of these parameters with respect to azimuthal angle ϕ.

in the topographic images is found to be close to 7 nm [19] for all V_g values.

The growth of ξ's as one approaches the Dirac point is in qualitative agreement with screening theory predictions. However, the abrupt changes in ξ (or $\xi_{1,2}$) when E_F approaches the Dirac point are not quite anticipated. Some fluctuations in ξ can be understood given that we are sampling a finite area. Figure 6 also shows $\xi_{1,2}$, calculated using the previously discussed screening theory, for different, but V_g independent, d and $n_{\rm imp}$ values. Thus it seems possible to describe $\xi_{1,2}$ variation with V_g by using V_g dependent d and $n_{\rm imp}$; however, modeling this V_g dependence is beyond the scope of this paper. The abrupt changes in $\xi_{1,2}$ in sample 1 close to $V_g = 40$ V and at $V_g = -20$ V, in sample 2, can arise from abrupt decrease in $n_{\rm imp}$, which will also be accompanied by an increase in d as predominantly the impurities close to graphene will change their state. In sample-2, $\xi_{1,2}$ seem to have an upturn near $V_g = 40$ V which can be directly correlated with the change in contrast of three dark spots, near the center of conductance map [19], into bright. Samaddar *et al.* [13], from their STM/S study, reported similar qualitative agreement with the screening theory together with some abrupt changes in ξ and an asymmetric variation of ξ about the Dirac point. The later can also be attributed to impurity-state change.

Since the studied samples are hole doped, due to interface defects, we expect majority of the charged interface defects to have negative charge. The presence of slight positive hysteresis [27], seen in the two probe resistance with V_g [19], indicates that interface defects do change their charge state although the converse need not be true. One can also analyze the defect's charge-state change in terms of change in the filling of the defect states that are distributed relative to the graphene Fermi energy [24]. In equilibrium the defect states up to graphene Fermi energy will be filled [16]. Thus the interface states that can possibly change their filling due to V_g change will be close to E_F.

VI. CONCLUSIONS

In conclusion, the interface defects, which are responsible for electronic inhomogeneities in graphene, are observed to change their charge state with change in back gate voltage. This also contributes to the evolution of graphene's electronic inhomogeneity other than the carrier density dependent screening physics. The change in defect state is predominantly seen when the graphene Fermi energy is close to the Dirac point. This implies that the defect's ionization energies are close to the graphene's Dirac point energy. Further, close to the Dirac point, where the screening of the impurity potential in graphene is extremely weak, the electronic inhomogeneity in graphene is described by two different length scales.

ACKNOWLEDGMENTS

We thank Sayanti Samaddar for careful reading of the manuscript and discussions. Financial support from the SERB-DST of the Government of India and from IIT Kanpur are gratefully acknowledged.

[1] J. Martin, N. Akerman, G. Ulbricht, T. Lohmann, J. H. Smet, K. von Klitzing, and A. Yacoby, Nat. Phys. **4**, 144 (2008).
[2] Y. Zhang, V. W. Brar, C. Girit, Alex Zettl, and M. F. Crommie, Nat. Phys. **5**, 722 (2009).
[3] A. Deshpande, W. Bao, F. Miao, C. N. Lau, and B. J. LeRoy, Phys. Rev. B **79**, 205411 (2009).
[4] A. Deshpande, W. Bao, Z. Zhao, C. N. Lau, and B. J. LeRoy, Phys. Rev. B **83**, 155409 (2011).
[5] A. S. Mayorov, D. C. Elias, I. S. Mukhin, S. V. Morozov, L. A. Ponomarenko, K. S. Novoselov, A. K. Geim, and R. V. Gorbachev, Nano Lett. **12**, 4629 (2012).
[6] A. Veligura, P. J. Zomer, I. J. Vera-Marun, C. Józsa, P. I. Gordiichuk, and B. J. Van-Wees, J. Appl. Phy. **110**, 113708 (2011).
[7] M. Gibertini, A. Tomadin, F. Guinea, M. I. Katsnelson, and M. Polini, Phys. Rev. B **85**, 201405(R) (2012).
[8] T. Ando, J. Phys. Soc. Jpn. **75**, 074716 (2006).
[9] M. I. Katsnelson, Phys. Rev. B **74**, 201401(R) (2006).
[10] Shaffique Adam, E. H. Hwang, V. M. Galitski, and S. D. Sarma, PNAS **104**, 18392 (2007).
[11] E. H. Hwang and S. Das Sarma, Phys. Rev. B **79**, 165404 (2009).

[12] S. Adam, S. Jung, N. N. Klimov, N. B. Zhitenev, J. A. Stroscio, and M. D. Stiles, Phys. Rev. B **84**, 235421 (2011).
[13] S. Samaddar, I. Yudhistira, S. Adam, H. Courtois, and C. B. Winkelmann, Phys. Rev. Lett. **116**, 126804 (2016).
[14] M. Ghaznavi, Z. L. Mišković, and F. O. Goodman, Phys. Rev. B **81**, 085416 (2010).
[15] A. K. Gupta, R. S. Sinha, and R. K. Singh, Rev. Sci. Instrum. **79**, 063701 (2008).
[16] A. K. Singh and A. K. Gupta, J. Phys. Condens. Matter **29**, 385302 (2017).
[17] S. K. Choudhary and A. K. Gupta, Appl. Phys. Lett. **98**, 102109 (2011).
[18] Y. Zhao, J. Wyrick, F. D. Natterer, J. F. Rodriguez-Nieva, C. Lewandowski, K. Watanabe, T. Taniguchi, L. S. Levitov, N. B. Zhitenev, and J. A. Stroscio, Science **348**, 672 (2015).
[19] See Supplemental Material at http://link.aps.org/supplemental/10.1103/PhysRevB.97.195415 for details on sample characterization, V_g dependent fits of the local spectra, STM/S maps of sample-2 with their analysis, and the linear screening theory.
[20] V. Geringer, M. Liebmann, T. Echtermeyer, S. Runte, M. Schmidt, R. Rückamp, M. C. Lemme, and M. Morgenstern, Phys. Rev. Lett. **102**, 076102 (2009).
[21] W. G. Cullen, M. Yamamoto, K. M. Burson, J. H. Chen, C. Jang, L. Li, M. S. Fuhrer, and E. D. Williams, Phys. Rev. Lett. **105**, 215504 (2010).
[22] H. E. Romero, N. Shen, P. Joshi, H. R. Gutierrez, S. A. Tadigadapa, J. O. Sofo, and P. C. Eklund, ACS Nano **2**, 2037 (2008).
[23] R. H. Miwa, T. M. Schmidt, W. L. Scopel, and A. Fazzio, Appl. Phys. Lett. **99**, 163108 (2011).
[24] B. Terres, L. A. Chizhova, F. Libisch, J. Peiro, D. Jorger, S. Engels, A. Girschik, K. Watanabe, T. Taniguchi, S. V. Rotkin, J. Burgdorfer, and C. Stampfer, Nat Commun. **7**, 11528 (2016).
[25] H. Xu, Y. Chen, J. Zhang, and H. Zhang, small **8**, 2833 (2012).
[26] E. Rossi, S. Adam, and S. Das Sarma, Phys. Rev. B **79**, 245423 (2009).
[27] H. Wang, Y. Wu, C. Cong, J. Shang, and T. Yu, ACS Nano **4**, 7221 (2010).